nature nanotechnology

Supplementary information

https://doi.org/10.1038/s41565-026-02270-6

Atomic-scale visualization of three-dimensional magnetization vectors with competing spin Hamiltonian interactions

In the format provided by the authors and unedited

Content

1. Methods 2

1.1 Extraction of EMCD in three dimensions with atomic-plane resolution 2

1.2 Data processing of EMCD spectra 7

1.3 Quantitative determination of 3D spin vectors 8

1.4 Inference of spin Hamiltonian energies 11

2. Theoretical simulation and experimental validation of in-plane components of 3D spin vectors with atomic-plane resolution 12

3. Robustness analysis of component-selective EMCD decomposition and spin-reorientation angles 15

3.1 Influence of sample thickness, tilting angle and virtual detector geometry on component-selective RSemcd 15

3.2 Influence of sample thickness, tilting angle and virtual detector geometry on spin-reorientation angles 16

4. Supplementary Figures and Tables 17

5. References 25

1. Methods

The analytical workflow used in this study is summarized in Figure S1. The workflow is divided into three sequential steps. First, a 4D-EMCD dataset is acquired experimentally, from which the A_x-, A_y- and A_z-channel Fe EMCD spectra are extracted. The corresponding component-resolved relative EMCD strengths constitute the direct experimental observables. Second, these experimentally extracted EMCD signals are converted into intrinsic M_x, M_y and M_z components by solving a system of linear equations with the coefficient matrix calculated by dynamical diffraction simulation. In this step, the simulated matrix is used to remove directional cross-talk and adjacent-plane delocalization, allowing the 3D spin vectors $\mathbf{S}_i$ to be determined for individual atomic planes. Third, the extracted atomic-plane spin vectors are applied into the established spin Hamiltonian equation to infer the exchange, Dzyaloshinskii–Moriya, Zeeman and single-ion anisotropy energy terms using established spin Hamiltonian constants.

The following sections describe, in order, how the component-resolved EMCD spectra are extracted from the 4D dataset, how simulated coefficient matrices are used to obtain intrinsic spin vector components, how these components are converted into 3D spin vectors, and how the extracted spin vectors are used to infer the spin Hamiltonian energy terms with atomic-plane resolution.

1.1 Extraction of EMCD in three dimensions with atomic-plane resolution

The magnetic component of the double differential cross-section (DDCS) in Eq. (11), which is also the experimental electron magnetic circular dichroism (EMCD) spectra $(S_+ - S_-)$, can be conceptualized as a linear combination of intrinsic magnetic circular dichroism spectra along the x, y and z directions, which arise from the $M_x(E)$, $M_y(E)$ and $M_z(E)$ components, respectively:

$$\left.\frac{\partial^2\sigma}{\partial E\partial\Omega}\right|_{Mag} = S_+ - S_- = \rho M_x(E) + \eta M_y(E) + \tau M_z(E), \qquad (12)$$

where S_+ and S_- represent the experimental electron energy-loss (EEL) spectra recorded at positive "+" and negative "-" positions, respectively. ρ, η, and τ represent the following dynamical diffraction coefficients,

$$\rho = \sum_{\mathbf{k},\mathbf{G}} 2|T_{\mathbf{G}}| \frac{G_y q_z - G_z q_y}{q^2 q'^2}, \qquad (13)$$

$$\eta = \sum_{\substack{\mathbf{k},\mathbf{G} \\ k_\perp < \frac{\alpha}{\lambda}}} \sin\frac{2\pi\Delta x}{d} \frac{G_z q_x - G_x q_z}{q^2 q'^2}, \qquad (14)$$

$$\tau = \sum_{\substack{\mathbf{k},\mathbf{G} \\ k_\perp < \frac{\alpha}{\lambda}}} \sin\frac{2\pi\Delta x}{d} \frac{G_x q_y - G_y q_x}{q^2 q'^2}, \qquad (15)$$

which determines the contributions of the $M_x(E)$, $M_y(E)$, and $M_z(E)$ components to the total measured signal. The magnetization vector $\mathbf{M}(E)$, the momentum transfer $\vec{q}$ and the reciprocal lattice vector $\mathbf{G}$, all of which are three-dimensional (3D) vectors, can be decomposed in the form $\mathbf{M}(E) = (M_x(E), M_y(E), M_z(E))$ in real space, $\mathbf{q} = (q_x, q_y, q_z)$ in momentum space and $\mathbf{G} = (G_x, G_y, G_z)$ in reciprocal lattice space, respectively, along the x, y, and z Cartesian directions.

In the experimental setup of beam-shift-based four-dimensional (4D) EMCD in Figure 1, the tunable parameters are the beam shift Δx in real space and the momentum transfer q_y in momentum space. We developed three different analysis strategies A_x, A_y and A_z to extract the EMCD spectra largely representing the $M_x(E)$, $M_y(E)$ and $M_z(E)$ components, respectively, from the 4D EMCD dataset using three linear combinations of signals $S(\Delta x, q_y, E)$ acquired at four symmetric points $(\pm\Delta x, \pm q_y)$ as shown in Figure 1e-1g.

The dynamical diffraction coefficient τ of the $M_z(E)$ component exhibits antisymmetric dependence on both the beam shift Δx in real space and the momentum transfer q_y in momentum space. According to this antisymmetric dependence, the following analysis strategy A_z is employed as $A_z = [S(\Delta x, q_y) + S(-\Delta x, -q_y)] - [S(\Delta x, -q_y) + S(-\Delta x, q_y)]$ as illustrated in Figure 1e. This A_z analysis strategy significantly increases the dynamical diffraction coefficient τ to enhance the sensitivity to the $M_z(E)$ component while largely canceling contributions from the $M_x(E)$ and $M_y(E)$ due to the antisymmetric dependence of their dynamical diffraction coefficients ρ and η on q_y only and Δx only, respectively. The term of $sin\frac{2\pi\Delta x}{d}\frac{-G_y q_x}{q^2 q'^2}$ in τ has antisymmetric dependence on Δx only, so it will also be largely canceled out when applying the A_z analysis

strategy. This operation yields a signal A_z mainly proportional to:

$$A_z \approx 4M_z(E)\frac{G_x q_y}{q^2 q'^2} sin\frac{2\pi\Delta x}{d}, \qquad (16)$$

According to Eq. (16), the experimental EMCD spectra $(S_+ - S_-)_{A_z}$ extracted by applying the A_z analysis strategy can be rewritten as

$$(S_+ - S_-)_{A_z} = \rho_{A_z} M_x(E) + \eta_{A_z} M_y(E) + \tau_{A_z} M_z(E), \qquad (17)$$

where ρ_{A_z}, η_{A_z}, and τ_{A_z} are the calculated dynamical diffraction coefficients ρ, η, and τ, respectively, when applying the A_z analysis strategy. Here the dynamical diffraction coefficient τ_{A_z} is dominant, while ρ_{A_z} and η_{A_z} are relatively insignificant.

Similarly, the $M_y(E)$ component, whose associated dynamic diffraction coefficient η is characterized by an antisymmetric dependence on the beam shift Δx and is independent of q_y, is targeted using the analysis strategy $A_y = [S(\Delta x, q_y) + S(\Delta x, -q_y)] - [S(-\Delta x, -q_y) + S(-\Delta x, q_y)]$, as illustrated in Figure 1f. This approach effectively increases the dynamical diffraction coefficient η to enhance the sensitivity to the $M_y(E)$ component. Contributions from the $M_x(E)$ and $M_z(E)$ components are largely canceled out, since their dynamical diffraction coefficients ρ and τ are antisymmetric in q_y. This results in a signal A_y approximately given by:

$$A_y \approx 4M_y(E)\frac{G_z q_x - G_x q_z}{q^2 q'^2} sin\frac{2\pi\Delta x}{d}, \qquad (18)$$

Consequently, the experimental EMCD spectra $(S_+ - S_-)_{A_y}$ extracted by applying the A_y analysis strategy is mainly dominated by the $\eta M_y(E)$, showing proportionality to $sin\frac{2\pi\Delta x}{d}$ and can be rewritten as:

$$(S_+ - S_-)_{A_y} = \rho_{A_y} M_x(E) + \eta_{A_y} M_y(E) + \tau_{A_y} M_z(E), \qquad (19)$$

where ρ_{A_y}, η_{A_y}, and τ_{A_y} are the calculated dynamical diffraction coefficients ρ, η, and τ, respectively, when applying the A_y analysis strategy. Here η_{A_y} is the dominant coefficient, while ρ_{A_y} and τ_{A_y} are relatively insignificant.

Finally, to detect the $M_x(E)$ component, which is associated with the dynamical diffraction coefficient α that is independent of the beam shift Δx but exhibits an antisymmetric dependence on momentum transfer q_y, the analysis strategy $A_x = [S(\Delta x, q_y) + S(-\Delta x, q_y)] - [S(\Delta x, -q_y) + S(-\Delta x, -q_y)]$ (Figure 1g) is implemented. This scheme is designed to enhance the sensitivity to the $M_x(E)$ component. The contributions from the $M_y(E)$ and $M_z(E)$ components with the dynamical diffraction coefficients η and τ having antisymmetric dependence on Δx are largely canceled out. Additionally, the term of $\frac{G_y q_z}{q^2 q'^2}$ in ρ is independent of Δx, so it will also be largely canceled out when applying the A_x analysis strategy. The magnetic signal with the A_x strategy was mainly dominant by the $\rho M_x(E)$ component with a dependence on $-q_y$. This yields a signal A_x approximately proportional to:

$$A_x \approx -8M_x(E)|T_G|\frac{G_z q_y}{q^2 q'^2}, \qquad (20)$$

According to Eq. (20), the experimental EMCD spectra $(S_+ - S_-)_{A_x}$ extracted by applying the A_x analysis strategy can be rewritten as

$$(S_+ - S_-)_{A_x} = \rho_{A_x} M_x(E) + \eta_{A_x} M_y(E) + \tau_{A_x} M_z(E), \qquad (21)$$

where ρ_{A_x}, η_{A_x}, and τ_{A_x} are the calculated dynamical diffraction coefficients ρ, η, and τ, respectively, when applying the A_x analysis strategy. Here ρ_{A_x} is the dominant dynamical

diffraction coefficient, while η_{A_x} and τ_{A_x} are insignificant.

By applying these A_x, A_y and A_z analysis strategies, the experimental EMCD spectra with dominant components of $M_x(E)$, $M_y(E)$, and $M_z(E)$ components, respectively, can be extracted atomic plane-by-plane from the 4D EMCD dataset and quantitatively described by equations (17), (19) and (21), respectively. With the calculated dynamical diffraction coefficients ρ, η, and τ under the experimental conditions and each analysis strategy, equations (17), (19), and (21) can be solved to extract the individual intrinsic magnetic components $M_x(E)$, $M_y(E)$, and $M_z(E)$ components without crosstalk among them.

According to the analysis strategies mentioned above, the A_z strategy can be applied to largely isolate the out-of-plane $M_z(E)$ component along the incident beam direction. We subtract the positive relative dynamical diffraction coefficient of EMCD (RC_{emcd}) signal integrated over specific q_y ranges at certain beam shifts, *e.g.*, the red rectangle II from -0.25d to -0.5d and the red rectangle III from 0.25d to 0.5d in Figure 3b, from the negative RC_{emcd} signal integrated over mirrored q_y ranges over the same beam shift ranges, *e.g.*, the blue rectangle I from -0.25d to -0.5d and the blue rectangle IV from 0.25d to 0.5d in Figure 3b. The beam-shift-dependent profiles of the integrated RC_{emcd} signal of $M_z(E)$ (Extended Data Fig. 3d), $M_y(E)$ (Extended Data Fig. 3c), and $M_x(E)$ (Extended Data Fig. 3b) are calculated from the difference in the integrated RC_{emcd} signal between the red and blue areas defined in the q_y domain in Extended Data Fig. 3i. By calculating the difference in the integrated RC_{emcd} signal between the beam shifts Δx in the red and blue areas in Extended Data Fig. 3d, the $M_z(E)$ contribution is maximized, while largely cancelling the $M_y(E)$ and $M_x(E)$ contributions. Assuming equal magnetic component strengths, Extended Data Fig. 3k indicates that the extracted signal is 92.9% of $M_z(E)$, with cross-talk of 6.7% of $M_y(E)$ and 0.4% of $M_x(E)$. Furthermore, for target atomic plane #5, ~88.8% of the $M_z(E)$ signal originates from that plane, while 4.9% and 6.2% originate from adjacent planes #4 and #6, respectively (Extended Data Fig. 3h), demonstrating a high degree of signal localization on the individual atomic plane.

The A_y strategy can be used to largely isolate the in-plane $M_y(E)$ component along the direction perpendicular to the incident beam and the plane normal $\mathbf{G}$. We subtract the RC_{emcd} signal integrated over all q_y at negative beam shifts from -0.25d to -0.5d in the red rectangle V from those integrated at positive beam shifts from 0.25d to 0.5d in the blue rectangle VI in Figure 3c. The RC_{emcd} signal of $M_y(E)$ is largely independent of q_y (Extended Data Fig. 3j), but is strongly antisymmetric with beam shift with respect to the atomic plane in these regions (Extended Data Fig. 3f). Meanwhile the RC_{emcd} signals of $M_x(E)$ (Extended Data Fig. 3e) and $M_z(E)$ (Extended Data Fig. 3g) with opposite signs for $\pm q_y$ are canceled out significantly. This A_y strategy shows high signal purity, with the desired $M_y(E)$ at ~90.7% and cross-talk of only ~0.7% of $M_x(E)$ and ~8.6% of $M_z(E)$ (Extended Data Fig. 3k), as well as relatively high localization, with ~84.9% of $M_y(E)$ from the target plane #5 (Extended Data Fig. 3h).

The A_x strategy can be utilized to largely isolate the in-plane $M_x(E)$ component along the plane normal $\mathbf{G}$ direction. We subtract the RC_{emcd} signal integrated over negative q_y in the red rectangle VII from that integrated over positive q_y in the blue rectangle VIII in Figure 3d, both within a symmetric beam shift range with respect to the atomic plane, *e.g.*, -0.3d to +0.3d. The RC_{emcd} signal for $M_x(E)$ exhibits the required opposite sign for $\pm q_y$ within the symmetric shift range in Extended Data Fig. 3b. Meanwhile, the RC_{emcd} signals for $M_y(E)$ (Extended Data Fig. 3c) and $M_x(E)$ (Extended Data Fig. 3d) tend to cancel due to their antisymmetry with respect to the atomic plane within the integration range of the beam shifts. Simulations suggest a signal purity of

82.4% for $M_x(E)$, with cross-talk of 13.3% for $M_y(E)$ and 4.3% for $M_z(E)$ (Extended Data Fig. 3k), as well as high localization, with 95.0% of the $M_x(E)$ signal from the target plane #5 (Extended Data Fig. 3h).

In the case of $YFeO_3$ under a three-beam condition (3BC) with the $\mathbf{G}_{(022)}$ systematic reflections excited, by using the A_x strategy with the dominant sensitivity to the $M_x(E)$ component, ten EMCD spectra of individual atomic plane are extracted from the 4D EMCD dataset. The relative strength of the EMCD (RS_{emcd}) on the odd-numbered (Extended Data Fig. 7a) and even-numbered (Extended Data Fig. 7b) spin sublattices were calculated to be -0.022±0.051 and -0.006±0.037, respectively, and indicate statistically insignificant intrinsic $M_x(E)$ components on both spin sublattices along the x direction in this experimental Cartesian coordinate system. Therefore, the intrinsic $M_x(E)$ component in this geometry is not considered in the following analysis to obtain the intrinsic $M_y(E)$ and $M_z(E)$ components and remove the crosstalk from other directions (Extended Data Fig. 3k) and the adjacent atomic planes (Extended Data Fig. 3h).

Here we define $M_{z,odd}(E)$ and $M_{z,even}(E)$ as the intrinsic components $M_z(E)$ of the odd-numbered and even-numbered spin sublattices, respectively, and define $M_{y,odd}(E)$ and $M_{y,even}(E)$ as the intrinsic $M_y(E)$ components of the odd-numbered and even-numbered spin sublattices, respectively, which can be used for the further analysis of magnetization vectors. By using the A_z and A_y strategies with the dominant sensitivity to the $M_z(E)$ and $M_y(E)$ components, respectively, ten sets of the experimental $(S_+ - S_-)_{\mathrm{A_z},i}$ and $(S_+ - S_-)_{\mathrm{A_y},i}$ EMCD spectra of individual atomic plane i, e.g. ranging from 1 to 10, are extracted from one 4D EMCD dataset. The summed experimental EMCD spectra of $(S_+ - S_-)_{\mathrm{A_z},odd}$ and $(S_+ - S_-)_{\mathrm{A_z},even}$ are summed over the EMCD spectra $(S_+ - S_-)_{\mathrm{A_z},i}$ on the odd-numbered and even-numbered spin sublattices, respectively. Meanwhile, the summed experimental EMCD spectra of $(S_+ - S_-)_{\mathrm{A_y},odd}$ and $(S_+ - S_-)_{\mathrm{A_y},even}$ are summed over the EMCD spectra $(S_+ - S_-)_{\mathrm{A_y},i}$ on the odd-numbered and even-numbered spin sublattices, respectively. The crosstalk from other directions (Extended Data Fig. 3k) and the adjacent atomic planes (Extended Data Fig. 3h) are inevitable, although the extracted EMCD spectra using the A_z and A_y strategies are dominantly sensitive to the $M_z(E)$ and $M_y(E)$ components, respectively. Considering these mutual crosstalk, the equation (17) to describe the summed experimental EMCD spectra $(S_+ - S_-)_{\mathrm{A_z},odd}$ and $(S_+ - S_-)_{\mathrm{A_z},even}$, and the equation (19) to describe the summed experimental EMCD spectra $(S_+ - S_-)_{\mathrm{A_y},odd}$ and $(S_+ - S_-)_{\mathrm{A_y},even}$ can be rewritten in the following way:

$$\begin{pmatrix} (S_+ - S_-)_{\mathrm{A_z},odd} \\ (S_+ - S_-)_{\mathrm{A_z},even} \\ (S_+ - S_-)_{\mathrm{A_y},odd} \\ (S_+ - S_-)_{\mathrm{A_y},even} \end{pmatrix} = C_{sim} \begin{pmatrix} M_{z,\mathrm{odd}}(E) \\ M_{z,\mathrm{even}}(E) \\ M_{y,\mathrm{odd}}(E) \\ M_{y,\mathrm{even}}(E) \end{pmatrix} \qquad (22)$$

where:

$$C_{\mathrm{sim}} = \begin{pmatrix} \tau_{A_z,\mathrm{odd}\to\mathrm{odd}} & \tau_{A_z,\mathrm{even}\to\mathrm{odd}} & \eta_{A_z,\mathrm{odd}\to\mathrm{odd}} & \eta_{A_z,\mathrm{even}\to\mathrm{odd}} \\ \tau_{A_z,\mathrm{odd}\to\mathrm{even}} & \tau_{A_z,\mathrm{even}\to\mathrm{even}} & \eta_{A_z,\mathrm{odd}\to\mathrm{even}} & \eta_{A_z,\mathrm{even}\to\mathrm{even}} \\ \tau_{A_y,\mathrm{odd}\to\mathrm{odd}} & \tau_{A_y,\mathrm{even}\to\mathrm{odd}} & \eta_{A_y,\mathrm{odd}\to\mathrm{odd}} & \eta_{A_y,\mathrm{even}\to\mathrm{odd}} \\ \tau_{A_y,\mathrm{odd}\to\mathrm{even}} & \tau_{A_y,\mathrm{even}\to\mathrm{even}} & \eta_{A_y,\mathrm{odd}\to\mathrm{even}} & \eta_{A_y,\mathrm{even}\to\mathrm{even}} \end{pmatrix} \qquad (23)$$

Here, C_{sim} is the simulated coefficient matrix assembled from the dynamical diffraction coefficients $\tau$and ηcalculated under the experimental diffraction geometry and the corresponding $A_z$and $A_y$analysis strategies. In the subscripts of η and τ, A_z and A_y mean that these two dynamical diffraction coefficients are calculated by using A_z and A_y strategies, respectively.

"*odd→even*" and "*even→even*" means that these two dynamical diffraction coefficients of the even-numbered spin sublattices are calculated by the contributions from the even-numbered spin sublattice itself and the adjacent odd-numbered spin sublattice, respectively. Similarly, "*odd→odd*" and "*even→odd*" means that these two dynamical diffraction coefficients of the odd-numbered spin sublattices are calculated by the contributions from the odd-numbered spin sublattice itself and the adjacent even-numbered spin sublattice, respectively.

The sublattice components removal of the crosstalk from the other spin sublattice and the magnetic components along the other directions are then obtained by directly solving Eq. (22):

$$\begin{pmatrix} M_{z,\mathrm{odd}}(E) \\ M_{z,\mathrm{even}}(E) \\ M_{y,\mathrm{odd}}(E) \\ M_{y,\mathrm{even}}(E) \end{pmatrix} = C_{sim}^{-1} \begin{pmatrix} (S_+ - S_-)_{\mathrm{A_z},odd} \\ (S_+ - S_-)_{\mathrm{A_z},even} \\ (S_+ - S_-)_{\mathrm{A_y},odd} \\ (S_+ - S_-)_{\mathrm{A_y},even} \end{pmatrix} \quad (24)$$

Therefore, the extraction of $M_{z,\mathrm{odd}}(E)$, $M_{z,\mathrm{even}}(E)$, $M_{y,\mathrm{odd}}(E)$, and $M_{y,\mathrm{even}}(E)$is a deterministic algebraic solution constrained by simulated scattering coefficients, rather than an iterative reconstruction or magnetic-model fitting. This algebraic workflow, converting the experimentally measured relative strength of EMCD $(S_+ - S_-)$ into intrinsic magnetic components $M(E)$, is schematically illustrated in Extended Data Fig. 10.

We would like to further extract the intrinsic magnetic $M_{y,i}(E)$ and $M_{z,i}(E)$ components of individual atomic plane i, e.g. ranging from 1 to 10, by removing the delocalized contributions of the adjacent atomic planes and the other directions. With the $\mathrm{A_y}$ and $\mathrm{A_z}$ analysis strategies, the combined delocalization contributions of the desired atomic plane itself and its two adjacent atomic planes to the desired atomic plane exceeds at least 97.9% and typically over 99% (Extended Data Fig. 3h). Therefore, approximately, we only consider the contributions from the target atomic plane itself and its two adjacent atomic planes when removing the delocalization effect. Here, the intrinsic $M_x(E)$ component in this geometry is not considered in the following analysis also. Considering these mutual crosstalk, the equations (17) and (19) to describe the experimental $(S_+ - S_-)_{\mathrm{A_z},i}$ and $(S_+ - S_-)_{\mathrm{A_y},i}$ EMCD spectra, respectively, of individual atomic plane i can be rewritten in the following way:

$$\begin{aligned}(S_+ - S_-)_{\mathrm{A_z},i} = {} & \eta_{\mathrm{A}_{\mathrm{z},i-1\to i}} M_{y,i-1}(E) + \eta_{\mathrm{A}_{\mathrm{z},i\to i}} M_{y,i}(E) + \eta_{\mathrm{A}_{\mathrm{z},i+1\to i}} M_{y,i+1}(E) + \tau_{\mathrm{A}_{\mathrm{z},i-1\to i}} M_{z,i-1}(E) \\ & + \tau_{\mathrm{A}_{\mathrm{z},i\to i}} M_{z,i}(E) + \tau_{\mathrm{A}_{\mathrm{z},i+1\to i}} M_{z,i+1}(E) \ , \quad (25)\end{aligned}$$

$$\begin{aligned}(S_+ - S_-)_{\mathrm{A_y},i} = {} & \eta_{\mathrm{A}_{\mathrm{y},i-1\to i}} M_{y,i-1}(E) + \eta_{\mathrm{A}_{\mathrm{y},i\to i}} M_{y,i}(E) + \eta_{\mathrm{A}_{\mathrm{y},i+1\to i}} M_{y,i+1}(E) \\ & + \tau_{\mathrm{A}_{\mathrm{y},i-1\to i}} M_{z,i-1}(E) + \tau_{\mathrm{A}_{\mathrm{y},i\to i}} M_{z,i}(E) + \tau_{\mathrm{A}_{\mathrm{y},i+1\to i}} M_{z,i+1}(E) \ , \quad (26)\end{aligned}$$

In the subscripts of η and τ, "*i-1 to i*", "*i to i*", and "*i+1 to i*" mean that these two dynamical diffraction coefficients of the individual atomic plane i are calculated by the contributions from the adjacent atomic plane $i-1$, the atomic plane i itself, and the adjacent atomic plane $i+1$, respectively. Here we do not need to know there is antiparallel or parallel magnetic moments in two spin sublattice, the delocalization coefficients of each spin lattice can be calculated quantitatively using dynamical diffraction calculations as shown in Extended Data Fig**.** 3h.

In the $YFeO_3$ under a 3BC with the $\mathbf{G}_{(022)}$ systematic reflections excited, the delocalization coefficients are almost identical regardless of whether *i* is even or odd. When calculating the $M_{y,i}(E)$ and $M_{z,i}(E)$ of the atomic planes 1 and *m*, where 1 and *m* are the number of the first and last atomic planes, respectively, in the experiment, there is no information about $M_{y,0}(E)$, $M_{z,0}(E)$, $M_{y,m+1}(E)$, and $M_{z,m+1}(E)$ beyond the acquisition area in experiments. Therefore, the intrinsic magnetic component $M_{y,even}(E)$ and $M_{z,even}(E)$ of the spin sublattice with all the even-

numbered atomic planes is considered as $M_{y,0}(E)$ and $M_{z,0}(E)$, respectively. Meanwhile, the individual intrinsic magnetic components $M_{y,odd}(E)$ and $M_{z,odd}(E)$ or $M_{y,even}(E)$ and $M_{z,even}(E)$ of the spin sublattices with the odd-numbered or even-numbered atomic planes are considered as $M_{y,m+1}(E)$ and $M_{z,m+1}(E)$ with the even-numbered or odd-numbered m, respectively. With the calculated dynamical diffraction coefficients under the experimental conditions, the system of equations (25) and (26) with the atomic plane number i ranging from 1 to m can be solved to extract the intrinsic $M_{z,i}(E)$ and $M_{y,i}(E)$ components of the individual atomic plane with number i without crosstalk from adjacent atomic planes and the magnetic components along the other two directions.

1.2 Data processing of EMCD spectra

The data processing steps for determining the $M_x(E)$, $M_y(E)$, and $M_z(E)$ components of 3D magnetization vectors projected along x, y, and z Cartesian directions from the 4D EMCD dataset using the A_x, A_y and A_z analysis strategies, respectively, are listed below.

Firstly, rigid shifting alignment was applied to the raw 4D EMCD dataset for correcting sample drift. The peak values of Gaussian fitting on the intensities of its annular dark-field (ADF) scanning transmission electron microscopy (STEM) images determine the positions of each atomic plane, which can also be used to determine the relative probe positions between two adjacent atomic planes.

Secondly, following the A_x, A_y and A_z analysis strategies as shown in Figures 3b-3d or Figures S2d-f, the "+" and "-" EEL spectra of individual atomic planes were extracted from the red rectangles and blue rectangles, respectively, with desired combinations of beam shifts Δx and momentum transfers q_y. For $YFeO_3$ under a 3BC with the $\mathbf{G}_{(022)}$ systematic reflections excited, the integration ranges of q_y in the 4D-EMCD dataset were selected from -12.4 mrad to 12.4 mrad (Extended Data Figure 3j) for the A_y analysis strategy and selected from -12.4 mrad to -3.7 mrad and from 3.7 mrad to 12.4 mrad (Extended Data Figure 3i) for the A_x and A_z analysis strategies. For $YFeO_3$ under a 3BC with the $\mathbf{G}_{(202)}$ systematic reflections excited, the integration ranges of q_y were selected from -14 mrad to 14 mrad (Figure S3h) for A_y analysis strategy and selected from -14 mrad to -2 mrad and from 2 mrad to 14 mrad (Figure S3d) for the A_x and A_z analysis strategies.

Thirdly, for pre-edge background subtraction, the data in the pre-edge region was fitted to a power-law model. The fitting parameters r of the "+" and "-" spectra of all the atomic planes were calculated from the sums of the "+" and "-" spectra, respectively, of all the atomic planes within the energy range from 610 eV to 700 eV and further applied to background subtraction for each atomic plane.

Fourthly, the energy-loss range from 703.7 eV to 730.3 eV at Fe L_3 and L_2 edges was selected for normalization of the "+" and "-" spectra of individual Fe atomic planes, which is different from the traditional post-edge normalization. There are two major reasons to choose the energy-loss range at Fe L_3 and L_2 edges for normalization. One is that the integral of the EMCD signals over the Fe L_3 and L_2 edges should be close to zero due to the sum rule of EMCD of Fe^{3+} ions with almost quenched orbital magnetic moments on octahedral sites in $YFeO_3$ with a pseudo-cubic structure.[1,2] In the case of $YFeO_3$ with a 3BC with the (022) systematic reflections excited, the Extended Data Fig. 8b and 8c show the EMCD spectra of $M_z(E)$ components of the odd-numbered and even-numbered spin sublattices, respectively, which were analyzed using the traditional post-edge normalization with the energy range from 730.3 eV to 760.3 eV. The EMCD spectra of all the atomic planes as shown

in the Extended Data Fig. 8d are achieved by subtracting the EMCD spectra of the odd-numbered atomic planes from those of the even-numbered atomic planes and are further used to calculate the orbital to spin magnetic moment ratio (m_L/m_S) of all Fe^{3+} ions in $YFeO_3$ as 0.046, experimentally demonstrating the almost quenched orbital magnetic moments of Fe^{3+} ions. The other reason is that the quantitative magnetic information calculated from the EMCD spectra by using the normalization energy ranges over Fe L_3 and L_2 edges are less sensitive to noises than that calculated from the EMCD spectra using the traditional post-edge normalization. The EMCD spectra of individual atomic planes were calculated by subtracting the corresponding "-" EEL spectra from the corresponding "+" EEL spectra after normalization.

1.3 Quantitative determination of 3D spin vectors

According to the sum rules of EMCD,[1,2] the spin and orbital sum rules for an EMCD experiment are expressed as

$$\frac{\int_{L_3}(S_+ - S_-)dE - 2\int_{L_2} S_+ - S_- dE}{\int_{L_3+L_2}(S_+ + S_-)dE} = \frac{C_{emcd}}{C_{NM}}\left(\frac{2}{3}\frac{\langle S_z\rangle}{N_h} + \frac{7}{3}\frac{\langle T_z\rangle}{N_h}\right) = RC_{emcd}\left(\frac{2}{3}\frac{\langle S_z\rangle}{N_h} + \frac{7}{3}\frac{\langle T_z\rangle}{N_h}\right), \quad (27)$$

$$\frac{\int_{L_3+L_2}(S_+ - S_-)dE}{\int_{L_3+L_2}(S_+ + S_-)dE} = \frac{C_{emcd}}{C_{NM}}\frac{1}{2}\frac{\langle L_Z\rangle}{N_h} = RC_{EMCD}\frac{1}{2}\frac{\langle L_Z\rangle}{N_h}, \quad (28)$$

where S_+ and S_- represent the experimental EEL spectra recorded at positive "+" and negative "-" positions, respectively. $\int_{L_3}(S_+ - S_-)dE$ and $\int_{L_2}(S_+ - S_-)dE$ are the energy integrals of the EMCD spectra $(S_+ - S_-)$ over the L_3 and L_2 edges, respectively, while $\int_{L_3+L_2}(S_+ + S_-)dE$ is the energy integral of the non-magnetic spectra $(S_+ + S_-)$ over the whole L_3 and L_2 edges. C_{NM} and C_{emcd} are the non-magnetic and EMCD parts, respectively, of the dynamical diffraction coefficients, while RC_{emcd} is the relative dynamical diffraction coefficient of EMCD, which can be determined by using dynamical diffraction calculations with the experimental conditions. $\langle S_z\rangle$, $\langle L_z\rangle$ and $\langle T_z\rangle$ are the ground-state expectation values of spin momentum, orbital momentum and magnetic-dipole operators, respectively, while N_h is the number of holes in the 3*d* orbital. In the pseudo-cubic $YFeO_3$, the magnetic dipole moment $\langle T_z\rangle$ can be neglected. The total magnetic moment $\langle\mu\rangle$ can be derived from the equations (27) and (28):

$$\langle\mu\rangle = -\mu_B(\langle L_Z\rangle + 2\langle S_z\rangle)$$

$$= -\mu_B\left[\left(\frac{2N_hC_{NM}}{C_{emcd}}\right)\frac{\int_{L_3+L_2}(S_+ - S_-)dE}{\int_{L_3+L_2}(S_+ + S_-)dE} + \left(\frac{3N_hC_{NM}}{C_{emcd}}\right)\frac{\int_{L_3}(S_+ - S_-)dE - 2\int_{L_2}(S_+ - S_-)dE}{\int_{L_3+L_2}(S_+ + S_-)dE}\right]$$

$$= \frac{-\mu_BN_hC_{NM}}{C_{emcd}} \times \frac{5\int_{L_3}(S_+ - S_-)dE - 4\int_{L_2}(S_+ - S_-)dE}{\int_{L_3+L_2}(S_+ + S_-)dE}, \quad (29)$$

Here RS_{emcd} representing the relative strength of EMCD is defined by:

$$RS_{emcd} = \frac{5\int_{L_3}(S_+ - S_-)dE - 4\int_{L_2}(S_+ - S_-)dE}{\int_{L_3+L_2}(S_+ + S_-)dE}, \quad (30)$$

Under the same acquisition conditions and analysis strategy leading to the same or similar C_{NM} and C_{emcd}, the total magnetic moment $\langle\mu\rangle$ is proportional to RS_{emcd}. Based on the experimental EMCD spectra $(S_+ - S_-)$ extracted by using A_x, A_y, and A_z analysis strategies, the $RS_{emcd,\,A_x}$, $RS_{emcd,\,A_y}$, and $RS_{emcd,\,A_z}$ can be calculated through Eq. (30) and largely represent the $M_x(E)$, $M_y(E)$, and $M_z(E)$ components, respectively, of the 3D magnetization vectors projected along x, y, and z Cartesian directions. The errors of the $RS_{emcd,\,A_x}$, $RS_{emcd,\,A_y}$, and $RS_{emcd,\,A_z}$ of each spin sublattice are determined by the standard error of the mean from the statistical analysis of the $RS_{emcd,\,A_x}$, $RS_{emcd,\,A_y}$, and $RS_{emcd,\,A_z}$, respectively, of all the individual atomic planes.

Following the procedures in the Section 1.1, we can extract the intrinsic $M_{z,odd}(E)$, $M_{z,even}(E)$, $M_{y,odd}(E)$, $M_{y,even}(E)$, $M_{x,odd}(E)$, and $M_{x,even}(E)$ components of the odd-numbered and even-numbered spin sublattices, as well as the intrinsic $M_{z,i}(E)$, $M_{y,i}(E)$, and $M_{x,i}(E)$ components of the individual atomic plane *i* after removing crosstalk from adjacent atomic planes and the magnetic components along the other two directions. These intrinsic magnetic components can be used to calculate the corresponding $RS_{emcd,\,M_{z,odd}}$, $RS_{emcd,\,M_{z,even}}$, $RS_{emcd,\,M_{y,odd}}$, $RS_{emcd,\,M_{y,even}}$, $RS_{emcd,\,M_{x,odd}}$, $RS_{emcd,\,M_{x,even}}$, $RS_{emcd,\,M_{z,i}}$, $RS_{emcd,\,M_{y,i}}$, and $RS_{emcd,\,M_{x,i}}$ through Eq. (30). These RS_{emcd} with the different subscripts represent the $M_x(E)$, $M_y(E)$ and $M_z(E)$ components of the 3D magnetization vectors of individual spin sublattice or individual atomic plane with number *i* projected along x, y, and z Cartesian directions without crosstalk from adjacent atomic planes and the magnetic components along other two directions. The errors of the $RS_{emcd,\,M_{x.odd}}$, $RS_{emcd,\,M_{x.even}}$, $RS_{emcd,\,M_y,odd}$, $RS_{emcd,\,M_y,even}$, $RS_{emcd,\,M_z,odd}$, and $RS_{emcd,\,M_z,even}$ of each spin sublattice are determined by the standard error of the mean from the statistical analysis of the $RS_{emcd,\,M_{x,i}}$, $RS_{emcd,\,M_{y,i}}$, and $RS_{emcd,\,M_{z,i}}$, respectively, of all the individual atomic planes. Additionally, according to the sum rules of EMCD, the orbital to spin moment ratio (m_L/m_S) can be calculated by the following equation[1,2]:

$$\frac{m_L}{m_s} = \frac{2}{3} \times \frac{\int_{L_3}(S_+ - S_-)dE + \int_{L_2}(S_+ - S_-)dE}{\int_{L_3}(S_+ - S_-)dE - \int_{L_2}(S_+ - S_-)dE} \quad , (31)$$

In an example of the spin sublattice *A*, since the measured $RS_{emcd,\,M_{z,odd}}$ and $RS_{emcd,\,M_{y,odd}}$ are directly proportional to the projections of the magnetic spin moments along the experimental *z* and *y* axes, respectively, the total magnetization vector $\mathbf{M_A}$ at the spin sublattice *A* can be determined via vector addition:

$$\mathbf{M_A} = RS_{emcd,\,M_z} \cdot \hat{e}_z + RS_{emcd,\,M_y} \cdot \hat{e}_y \,, (32)$$

where $\hat{e}_z$, $\hat{e}_y$, and $\hat{e}_x$ are the unit vectors in the experimental Cartesian coordinate system of $YFeO_3$ under 3BC with systematic reflections $\mathbf{G}_{(022)}$ excited, which is tilted away from the [100] zone axis by 7°. By converting this experimental Cartesian coordinate system into the crystallographic coordinate system, the $\hat{e}_z$ incident electron beam direction and the $\hat{e}_y$ direction are indexed as $[15, 1, \bar{1}]$ and $[\bar{1}\bar{5}5]$, respectively, while the $\hat{e}_x$ direction is $\mathbf{G}_{(022)}$ perpendicular to the (022) plane. Therefore, the crystallographic directions of the magnetic spin moments $\mathbf{M_A}$ and $\mathbf{M_B}$ at two antiferromagnetic (AFM) spin sublattices are determined as $[9, 1, \bar{1}]$ and $[\bar{5}\bar{1}1]$, respectively, by using the Equation (32) and rounding to the closest integer Miller indices.

To make the conversion from the intrinsic RS_{emcd} values to the derived spin vectors fully traceable, the numerical results are summarized in Table S2. Specifically, Table S2 lists the intrinsic RS_{emcd} values associated with the M_y and M_z components, the spin-vector directions derived in the experimental Cartesian coordinate system, the corresponding approximate Miller-index representations, the canting angles, and the canting angles projected on the crystallographic ac-

plane. Both the sublattice-averaged results for the odd- and even-numbered atomic planes and the representative individual atomic planes Nos. 1-3 are included. This table therefore provides a direct numerical link between the measured intrinsic EMCD components, the derived 3D spin directions, and the projected canting angles. As listed in Table S2, the 3D spin vectors $\mathbf{S}$ on each spin sublattice (Figure 5a) and each atomic plane, (*e.g.*, No. 1 to No. 3; Figure 5c) are derived from $\mathbf{S} = S\hat{n}$, where the Fe spin S=5/2 in the canted antiferromagnet $YFeO_3$,[3] and $\hat{n}$ is the unit vector along the direction of the magnetic spin moments on each spin sublattice, e.g. $[9, 1, \bar{1}]$ and $[\bar{5}\bar{1}1]$, and each atomic plane. The angles between a axis and 3D spin vectors of each spin sublattice defined as α and β are determined to be 11.6º±8.0° from [100] and 19.5º± 8.2° from $[\bar{1}00]$, respectively. The errors of α and β are estimated from the error values of the measured $RS_{emcd,\,M_z}$ and $RS_{emcd,\,M_y}$ of each spin sublattice by using error propagation.

1.4 Inference of spin Hamiltonian energies

Our methodology for inferring the spin Hamiltonian energy at the atomic-plane level is a "bottom-up" approach, building directly from experimentally measured atomic-scale 3D spin vectors, atomic structures and established coefficient. By utilizing the quantitative 3D spin vectors ($\mathbf{S_i}$ and $\mathbf{S_j}$) derived from our 4D-EMCD measurements atomic plane-by-plane, we infer the four energy contributions to a spin Hamiltonian, including symmetric super-exchange Hamiltonian ($\mathcal{H}_{ex}$), antisymmetric Dzyaloshinskii-Moriya Hamiltonian ($\mathcal{H}_{DM}$), Zeeman Hamiltonian ($\mathcal{H}_z$), and single-ion anisotropy (SIA) Hamiltonian ($\mathcal{H}_{sia}$).

1.4.1 Symmetric Super-exchange Hamiltonian ($\mathcal{H}_{ex}$)

First, we infer the energy contribution of the symmetric Heisenberg $\mathcal{H}_{ex}$, which is the dominant term establishing the fundamental G-type AFM order. The $\mathcal{H}_{ex}$ energies per Fe atom between Fe atoms on two spin sublattices or two adjacent atomic planes are calculated by

$$\mathcal{H}_{ex} = -\frac{1}{2}\sum_{i,j} J_{ij}\mathbf{S_i}\cdot\mathbf{S_j} \quad (33)$$

where $\mathbf{S_i}$ and $\mathbf{S_j}$ are the 3D spin vectors $\mathbf{S}$ of Fe atoms located on two spin sublattices or two adjacent atomic planes . The nearest-neighbor exchange constant J is set as -4.77 meV, which was derived from experimental data in single-crystalline $YFeO_3$.[3] Based on our measured spin vectors on two spin sublattices, the $\mathcal{H}_{ex}$ energy per Fe atom pair between Fe atoms on two spin sublattices is -29.09±1.33 meV/atom pair. The error of the $\mathcal{H}_{ex}$ energy per Fe atom pair is inferred by the standard error of the mean from the statistical analysis of the $\mathcal{H}_{ex}$ energies per Fe atom pair between Fe atoms on each pair of two adjacent atomic planes among all the individual atomic planes.

1.4.2 Antisymmetric Dzyaloshinskii-Moriya Hamiltonian ($\mathcal{H}_{DM}$)

Secondly, we infer the energy contribution of the antisymmetric $\mathcal{H}_{DM}$, which governs the subtle spin canting between neighboring magnetic spin moments. The $\mathcal{H}_{DM}$ energies per Fe atom between Fe atoms on two spin sublattices or two adjacent atomic planes are calculated by

$$\mathcal{H}_{DM} = \frac{1}{2}\sum_{i,j} \mathbf{D_{ij}}\cdot(\mathbf{S_i}\times\mathbf{S_j}) \quad (34)$$

where $\mathbf{D_{ij}}$ is the local Dzyaloshinskii-Moriya interaction (DMI) vector constrained by crystal symmetry of $YFeO_3$. For the given two spin sublattices or two adjacent atomic planes, $\mathbf{S_i}$ and $\mathbf{S_j}$ are fixed. The $\sum_{i,j}\mathbf{D_{ij}}$ summed over two AFM spin sublattices was derived from the sum of six non-equivalent experimental $\mathbf{D_{ij}}$ in single-crystalline $YFeO_3$[3] and was inferred as (0, 0.62, 0) meV.

Based on our measured spin vectors on two spin sublattices, the $\mathcal{H}_{DM}$ energy per Fe atom pair between Fe atoms on two spin sublattices is -0.43±0.51 meV/atom pair. The error of the $\mathcal{H}_{DM}$ energy per Fe atom pair is inferred by the standard error of the mean from the statistical analysis of the $\mathcal{H}_{DM}$ energies per Fe atom pair between Fe atoms on each pair of two adjacent atomic planes among all the individual atomic planes.

1.4.3 Zeeman Hamiltonian ($\mathcal{H}_z$)

Thirdly, we infer the energy contribution of the $\mathcal{H}_z$, which accounts for the spin interaction with an external magnetic field *H* along a unit direction $\vec{H}$. The $\mathcal{H}_z$ energies per Fe atom of Fe atoms on the individual atomic planes are calculated by

$\mathcal{H}_z = -\mu_B \mu_0 H \sum_i \mathbf{H} \cdot \mathbf{S_i}$ (35)

where μ_B represents the Bohr magneton as 9.274 x 10^{-24} J/T, $\mu_0 H$ denotes the strength of the external magnetic field of 2.5 T in the experiments, $\mathbf{H}$ is the unit vector along the $[15, 1, \bar{1}]$ direction of the applied external magnetic field, and the effective magnetic moment of the Fe atom is inferred as 3.6 μ_B based on our DFT calculations. The resulting energy values are converted from Joules to millielectronvolts (meV) for consistency with other energy terms. Based on our measured spin vectors on two spin sublattices, the $\mathcal{H}_z$ energies for each spin sublattice are inferred to be 1.271±0.007 and -1.368±0.050 meV/atom. The errors of the $\mathcal{H}_z$ energy per Fe atom are inferred by the standard error of the mean from the statistical analysis of the $\mathcal{H}_z$ energies per Fe atom of Fe atoms on the individual atomic planes.

1.4.4 Single-Ion Anisotropy Hamiltonian ($\mathcal{H}_{sia}$)

Finally, we infer the energy contribution of the $\mathcal{H}_{sia}$, which favors spin alignment along a crystallographic easy axis, e.g. the *a*-axis in $YFeO_3$, or an intermediate anisotropy axis, e.g. the *c*-axis in $YFeO_3$. The $\mathcal{H}_{sia}$ energies per Fe atom of Fe atoms on the individual atomic planes are calculated by

$H_{sia} = H_{sia,a} + H_{sia,c} = -K_a \sum_i {S_{ia}}^2 - K_c \sum_i {S_{ic}}^2$ (36)

where $\mathcal{H}_{sia,a}$ and $\mathcal{H}_{sia,c}$ are the $\mathcal{H}_{sia}$ favoring spin along the *a* and *c* axes, respectively, K_a and K_c denote the anisotropy constants along the crystallographic *a* and *c* axes, respectively, while the variables S_{ia} and S_{ic} refer to the projections of the spin vector $\mathbf{S_i}$ onto the *a* and *c* axes, respectively, in $YFeO_3$. The K_a and K_c are set as 0.0052 and 0.0044 meV, respectively, which were derived from experimental data in single-crystalline $YFeO_3$.[3] Based on our measured spin vectors on two spin sublattices, the $\mathcal{H}_{sia,a}$ energies for each spin sublattice are inferred to be -28.8±1.0×10^{-3} and -31.2±2.0×10^{-3} meV/atom , while the $\mathcal{H}_{sia,c}$ energies for each spin sublattice are inferred to be -2.0±0.7×10^{-3} and -0.7±1.0×10^{-3} meV/atom. The errors of the $\mathcal{H}_{sia,a}$ and $\mathcal{H}_{sia,c}$ energies per Fe atom are inferred by the standard error of the mean from the statistical analysis of the $\mathcal{H}_{sia,a}$ and $\mathcal{H}_{sia,c}$ energies, respectively, per Fe atom of Fe atoms on the individual atomic planes.

This comprehensive approach enables us to spatially map the variations of individual energy contributions of $\mathcal{H}_{ex}$, $\mathcal{H}_{DM}$, $\mathcal{H}_z$, and $\mathcal{H}_{sia}$ at the atomic-plane level, providing a significant advantage over traditional "top-down" approaches that infer only average values from macroscopic phenomena.

2. Theoretical simulation and experimental validation of in-plane components of 3D spin vectors with atomic-plane resolution

In the experimental Cartesian coordinate system of $YFeO_3$ under a 3BC with the (202) systematic reflections excited for validating the A_y and A_x analysis strategies, the z and y directions are about 8° away from [010] and $[10\bar{1}]$, respectively, as the x direction is the surface normal $\mathbf{G}_{(202)}$ of the (202) crystallographic plane (Figures S2a-2c). Consequently, the Fe spin vectors, known to be predominantly along [100] from prior experiments, are expected to project significantly onto both the in-plane x and y directions with an angle of about 35° and 55°, respectively. The 4D EMCD datasets of $YFeO_3$ under a 3BC with the (202) systematic reflections excited were acquired using the same convergence semi-angle of 8.95 mrad at 300 kV. The sample thickness was measured as 20 nm by its low-loss EEL spectra as shown in Extended Data Fig. 4f. The drift-corrected ADF STEM image (Extended Data Fig. 9a) shows nine consecutive (202) planes with a 2.17 Å interplanar spacing. These planes exhibit pairs of double bright lines, which correspond to Y atomic planes, with intervening less bright and dark lines that correspond to Fe atomic plane. The less bright lines and dark lines correlate with the odd-numbered and even-numbered Fe (202) atomic planes, respectively. The odd-numbered and even-numbered Fe (202) planes are at a distance of 0.58 Å and 0.62 Å, respectively, from adjacent oxygen planes. Their crystallographic non-equivalence, stemming from differing proximities to oxygen atoms was further confirmed by the simulated ADF STEM image (Extended Data Fig. 9a). The atomic-resolution energy dispersive X-ray spectroscopy (EDS) mapping in the same experimental condition as the one to acquire the 4D EMCD dataset further demonstrates that Y atomic planes in blue (Extended Data Figs. 9a, 4b, and 4d) correspond to the double bright lines, while the Fe atomic planes in green correspond to the less bright lines within the double bright lines and the dark lines between them. As shown in Figure S2c, the diffraction disk of $\vec{G}_{(202)}$ aligned parallel to the q_x direction allowed us to achieve q_y-dependent electron energy loss spectroscopy (EELS) imaging in the 4D EMCD dataset, while the typical $\mathbf{G}_{(101)}$ diffraction disks, indicated by the arrow, were observed as expected theoretically.

Assuming no prior knowledge of the direction of the Néel vector $\mathbf{L}$, it is also assumed that the antiparallel magnetization vectors $\mathbf{M_A}$ and $\mathbf{M_B}$ on the AFM spin sublattices have the opposite M_x, M_y, and M_z along x, y, and z directions, respectively (Figure S2a). The magnetization vectors of the atomic plane with the beam shift of 0 are antiparallel to those of adjacent atomic planes with the beam shift of $d_{(202)}$ or $-d_{(202)}$, where the interplanar distance of (202) planes $d_{(202)}$ is 2.17 Å, and the beam shift of the convergent electron probe with the unit of $d_{(202)}$ is defined as the distance between probe position and the specific Fe (202) plane. The beam-shift-dependent distributions of the relative dynamical diffraction coefficient of EMCD (RC_{emcd}) of $M_z(E)$ (Figure S2d), $M_y(E)$ (Figure S2e), and $M_x(E)$ (Figure S2f) at the diffraction planes of a 20 nm thick $YFeO_3$ under a 3BC with the (202) systematic reflections excited at an acceleration voltage of 300 kV with a convergence semi-angle of 8.95 mrad were simulated by using dynamical diffraction simulations. Apparently, the three same analysis strategies A_z, A_y, and A_x (Figures S2d-2f) could also be applied to extract the EMCD spectra mainly representing the $M_z(E)$, $M_y(E)$, and $M_x(E)$ components, respectively, of 3D magnetization vectors $\mathbf{M_A}$ and $\mathbf{M_B}$ on each spin sublattice atomic plane by atomic plane.

To quantify the $M_y(E)$ specificity using A_y analysis strategy, the beam-shift-dependent profiles of integrated RC_{emcd} of $M_x(E)$ (Figure S3e), $M_y(E)$ (Figure S3f), $M_z(E)$ (Figure S3g) were calculated from the integrated RC_{emcd} at the range of q_y covered with dark green in Figure S3h. In addition, to quantify the $M_x(E)$ and $M_z(E)$ specificity when using A_x and A_z analysis strategies, respectively, the beam shift-dependent profiles of integrated RC_{emcd} of $M_x(E)$ (Figure S3a), $M_y(E)$ (Figure S3b), $M_z(E)$ (Figure S3c) are calculated from the difference in the integrated RC_{emcd} between the red and blue areas in q_y in Figure S3d. Equal strengths of $M_x(E)$, $M_y(E)$, and $M_z(E)$ were assumed here in the dynamical diffraction simulation. It is worth noting that the even-numbered and odd-numbered Fe (202) atomic planes are not crystallographically equivalent as shown in Figure S3a due to the altermagnetic symmetry of $YFeO_3$. In the example of the Fe (202) atomic plane No. 3 marked by pink, $M_x(E)$, $M_y(E)$, and $M_z(E)$ dominantly contribute to 85.8%, 97.2%, and 86.2%, respectively, of total integrated RC_{emcd} simulated by using the A_x, A_y, and A_z analysis strategies, respectively, as shown in Figure S3k. Meanwhile, the 90.8% of $M_x(E)$, 87.1% of $M_y(E)$, and 88.9% of $M_z(E)$ of total integrated RC_{emcd} come from the atomic plane No. 3 itself by using the A_x, A_y, and A_z analysis strategies, respectively, as shown in Figure S3j. In the example of the Fe (202) atomic plane No. 4 marked by yellow, the $M_x(E)$, $M_y(E)$, and $M_z(E)$ dominantly contributes to 89.8%, 93.4%, and 84.8%, respectively, of total integrated RC_{emcd} acquired by using the A_x, A_y, and A_z analysis strategies, respectively, as shown in Figure S3k. Meanwhile, the 89.8% of $M_x(E)$, 77.2% of $M_y(E)$, and 78.6% of $M_z(E)$ of total integrated RC_{emcd} come from the atomic plane No. 4 itself by using the A_x, A_y, and A_z analysis strategies, respectively, as shown in Figure S3i. The relevant EMCD experimental results have been discussed in the main text.

In case of $YFeO_3$ under 3BC tilted away from the [010] zone axis with the dominant $M_y(E)$ and $M_x(E)$ components in the 3D spin vectors, the corresponding EMCD $(S_+ - S_-)_{A_y}$ (Figure S4), EMCD $(S_+ - S_-)_{A_x}$ spectra (Figure S5) and EMCD $(S_+ - S_-)_{A_z}$ spectra (Figure S6) from the nine Fe (202) atomic planes were extracted using the A_y (Figure S2e), A_x (cf. Figure S2f), and A_z (cf. Figure S2d) analysis strategies, respectively. By using the A_y analysis strategy with the dominant sensitivity to the $M_y(E)$ component, the sum of the EMCD spectra extracted from all odd-numbered planes (Figure S4a) and that extracted from all even-numbered planes (Figure S4b) reveal a clear inversion of the EMCD signals of Fe atoms on two spin sublattices. The RS_{emcd} signals calculated from all nine atomic planes mainly represent the projected strength of magnetic spin moments along the y axis oscillating between positive and negative values, demonstrating the inversion of the Fe EMCD signals between each pair of adjacent planes, while one exception at Fe (202) plane 1 along the y direction may arise from a measurement error. The quantitative RS_{emcd} with the dominant $M_y(E)$ component on the odd-numbered and even-numbered spin sublattices were calculated as -0.092±0.013 and 0.074±0.004, respectively. The errors of the RS_{emcd} of each spin sublattice are determined by the standard error of the mean from the statistical analysis of the RS_{emcd} of the individual odd-numbered and even-numbered atomic planes. All the experimental results mentioned above confirm AFM coupling of Fe atoms between adjacent planes along the y direction in $YFeO_3$ under 3BC tilted away from the [010] zone axis.

By using the A_x analysis strategy with the dominant sensitivity to the $M_x(E)$ component, the sum of the EMCD spectra extracted from all odd-numbered planes (Figure S5a) demonstrates a robust EMCD-like spectral signature with negative and positive signals at the L_3 and L_2 peaks, while the sum of Fe EMCD spectra extracted from all even-numbered planes (Figure S5b) shows the very

weak EMCD signals close to the noise level. The RS_{emcd} signals calculated from the atomic planes generally also represent the projected strength of magnetic spin moments along the *x* axis oscillating between the positive and negative values, with a notable exception at plane No. 6. This local deviation and the overall lower signal-to-noise ratio primarily arise from the relatively small dynamical diffraction coefficients inherent to this specific scattering geometry. Nevertheless, the experimental results with the oscillating strengths support the presence of AFM order along *x* direction. Future investigations focusing on optimizing these dynamical coefficients will further enhance the sensitivity and precision for such weak magnetic components.

By using the A_z analysis strategy with the dominant sensitivity to the $M_z(E)$ component, the signs of the extracted EMCD spectra appear random across the planes (Figure S6). Consequently, the RS_{emcd} of 0.011±0.031 and 0.014±0.015 calculated from the summed signals on both odd-numbered and even-numbered planes, respectively, are statistically insignificant. The insignificant intrinsic $M_z(E)$ component further validate that no obvious spin rotation occurs towards the 2.5 T external field applied along the out-of-plane *z* direction of $[1,12,\bar{1}]$ close to the AFM hard *b*-axis. This is consistent with the theoretical expectation due to magnetic anisotropy.

The successful observation of AFM coupling of the magnetic spin moments along both *x* and *y* axes, combined with the experimentally confirmed insignificant $M_z(E)$ component, is fully consistent with the projected magnetic structure of $YFeO_3$ in this specific orientation. Collectively, these results demonstrate the validity and effectiveness of our beam-shift-based 4D-EMCD technique to detect in-plane components of 3D spin vectors with atomic-plane resolution.

3. Robustness analysis of component-selective EMCD decomposition and spin-reorientation angles

To evaluate the robustness of the component-selective EMCD decomposition and spin-reorientation angles, we performed a quantitative analysis of their sensitivity to sample thickness, tilting angle, and virtual detector geometry. These tests were designed to assess how sensitive experimental perturbations may affect the dynamical diffraction coefficients, the analyzed component-selective relative EMCD strengths RS_{emcd}, and the spin-reorientation angles.

3.1 Influence of sample thickness, tilting angle and virtual detector geometry on component-selective RS_{emcd}

We first examined the effect of sample thickness on the extracted intrinsic RS_{emcd}values for the M_z and M_y components. We selected the sample thickness of 16.8 nm, which was experimentally measured with the precision of 0.5 nm via position averaged convergent beam electron diffraction using convolutional neural networks.[4] Considering the thickness measurement precision, we tested thickness of 14.8, 16.8 and 18.8 nm to evaluate the sensitivity to thickness uncertainty of ±2 nm. The thickness variation changes $M_{z,odd}$, $M_{z,even}$, $M_{y,odd}$ and $M_{y,even}$ by 3.3%, 2.5%, 5.4% and 6.2%, respectively, at most (Figure S7a).

We next examined the sensitivity to tilting angles away from Laue center under a 3BC. The experimental tilting angle of 7° was selected with the variation of ± 0.5°, considering the angular

precision of the goniometer stage in our microscope. The maximum relative changes are 8.8% for $M_{z,odd}$, 7.0% for $M_{z,even}$, 4.8% for $M_{y,odd}$ and 11.7% for $M_{y,even}$ at most (Figure S7b). Although the relative change for $M_{y,even}$ appears larger, this is mainly because the absolute value of $M_{y,even}$ is close to zero. The corresponding absolute variation of $M_{y,even}$ remains small.

Finally, we evaluated the influence of virtual detector geometry by varying the Δq_y selection, which is defined and marked in the Extended Data Fig. 3i. Considering that the pixel size of q_y in the q-E image is about 0.037 mrad, here we choose Δq_y of ±0.125 mrad, which is about three pixel sizes for estimating the experimental q_y uncertainty. This Δq_y perturbation changes $M_{z,odd}$ and $M_{z,even}$ by 3.85% and 12.7%, respectively, at most (Figure S7c). The q_y-independent M_y components were extracted using the whole q_y range, so it is not considered in error analysis here.

3.2 Influence of sample thickness, tilting angle and virtual detector geometry on spin-reorientation angles

We further investigated the influence of sample thickness, tilting angle, and virtual detector geometry as described above to the spin-reorientation angles α_1 for odd-numbered atomic planes and β_1 for even-numbered atomic planes. As shown in Figures S7d-f and Table S1, thickness variations lead to errors $\sigma_{\Delta t}$ of 0.21°for α_1 and 0.24° for β_1 at most, tilting angle variations lead to errors $\sigma_{\Delta\theta}$ of 0.75° for $\alpha_1$and 0.17° for β_1 at most, while the Δq_y perturbations lead to errors $\sigma_{\Delta q_y}$ of 0.21° for α_1 and 0.11° for β_1 at most. The total error was estimated as

$$\sigma_{total} = \sqrt{\sigma_{noise}^2 + \sigma_{\Delta t}^2 + \sigma_{\Delta\theta}^2 + \sigma_{\Delta q_y}^2}. \quad (37)$$

The total errors give 7.84° for α_1 and 6.91° for β_1, which are very close to the statistical errors σ_{noise} from experimental spectrum noises of 7.8° for α_1 and 6.9° for β_1, as summarized in Table S1. The 99 % of the total errors in the spin-reorientation angles come from experimental spectrum noises rather than the perturbations in sample thickness, tilting angle and virtual detector geometry. The robustness of the spin-reorientation angles to the perturbations in sample thickness, tilting angle, and virtual detector geometry is demonstrated quantitatively.

4. Supplementary Figures and Tables

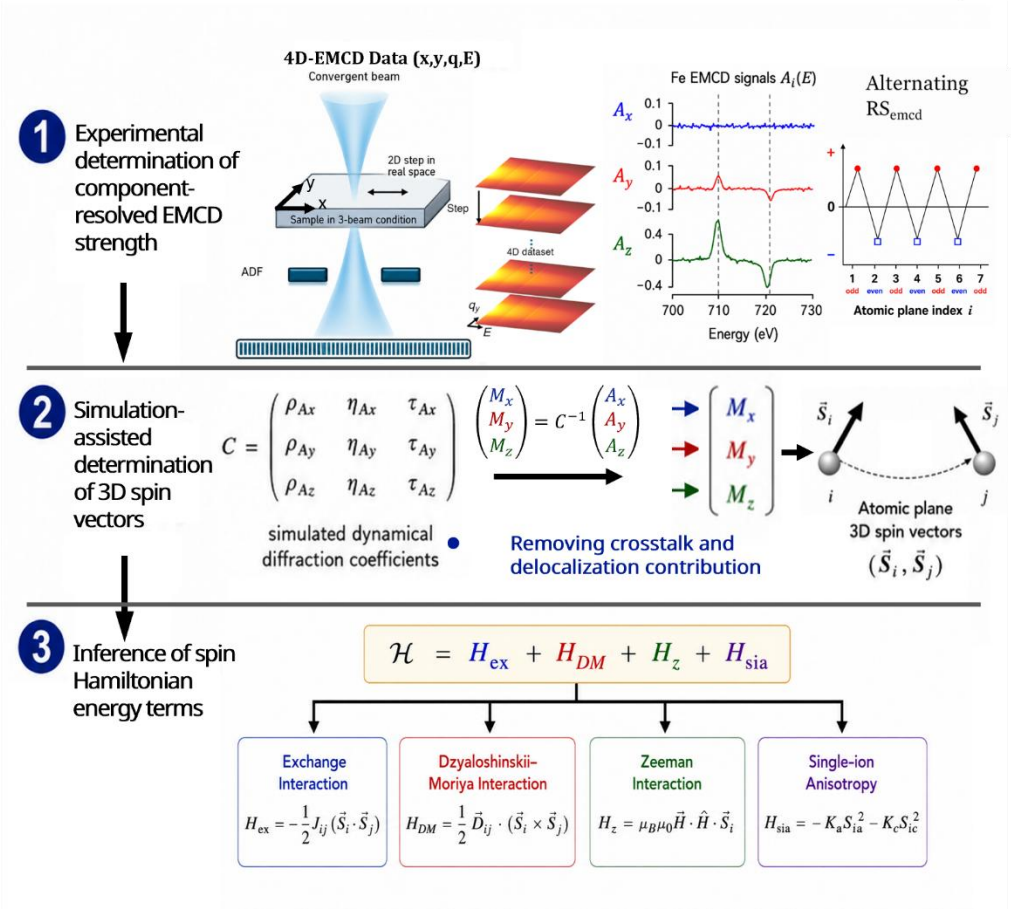


Figure S1 Data processing and quantitative analysis of four-dimensional electron magnetic circular dichroism (4D-EMCD) dataset to achieve three-dimensional spin vectors and infer the spin Hamiltonian energy terms with atomic-plane resolution.

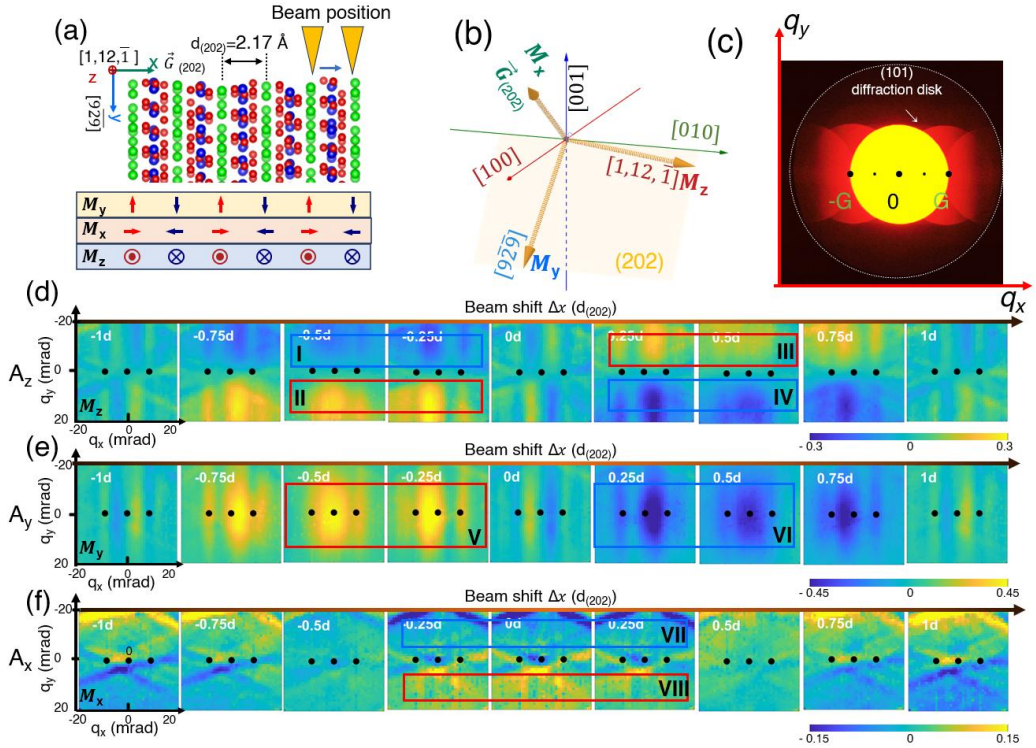


Figure S2 (a) Top view of the structural model, (b) the corresponding experimental Cartesian coordinate system, and (c) the typical diffraction pattern of $YFeO_3$ under a three-beam condition (3BC) with the $\mathbf{G}_{(202)}$ systematic reflections excited. The y direction and the incident electron beam z direction are $[9\bar{2}\bar{9}]$ away from $[10\bar{1}]$ by ~8° and $[1,12,\bar{1}]$ away from [010] by ~8°, respectively, while the x direction is $\mathbf{G}_{(202)}$ perpendicular to the Fe (202) planes with antiferromagnetic coupling. The incident electron beam comes from z direction and scans along x direction as indicated by the yellow cones with an arrow in (a). The white arrow in (c) indicates the characteristic $\mathbf{G}_{(101)}$ diffraction disk along this direction, further verifying the 3BC with the $\mathbf{G}_{(202)}$ systematic reflections excited. The q_x and q_y axes are parallel and perpendicular, respectively, to the $\mathbf{G}_{(202)}$ vector. The beam-shift-dependent distributions of the relative dynamical diffraction coefficient of EMCD (RC_{emcd}) of the (d) $M_z(E)$, (e) $M_y(E)$, and (f) $M_x(E)$ components along the q_x and q_y directions in the diffraction plane as the function of the beam shift Δx ranging from -1$d_{(202)}$ to 1$d_{(202)}$ with a step of 0.25$d_{(202)}$. Similarly, following the theoretical prediction in Figs. 1e-g, three analysis strategies A_z, A_y, and A_x by subtracting the EMCD signals acquired at the positive boxes (labeled II and III, V, VIII) in red from those acquired at the negative boxes (labeled I and IV, VI, VII) in blue are marked to largely isolate the $M_z(E)$, $M_y(E)$, and $M_x(E)$ components, respectively, and minimize their mutual crosstalk. Three black dots in each beam shift-dependent distribution of RC_{emcd} denote the center positions of $\mathbf{G}_{(\bar{2}0\bar{2})}$, transmitted disk and $\mathbf{G}_{(202)}$.

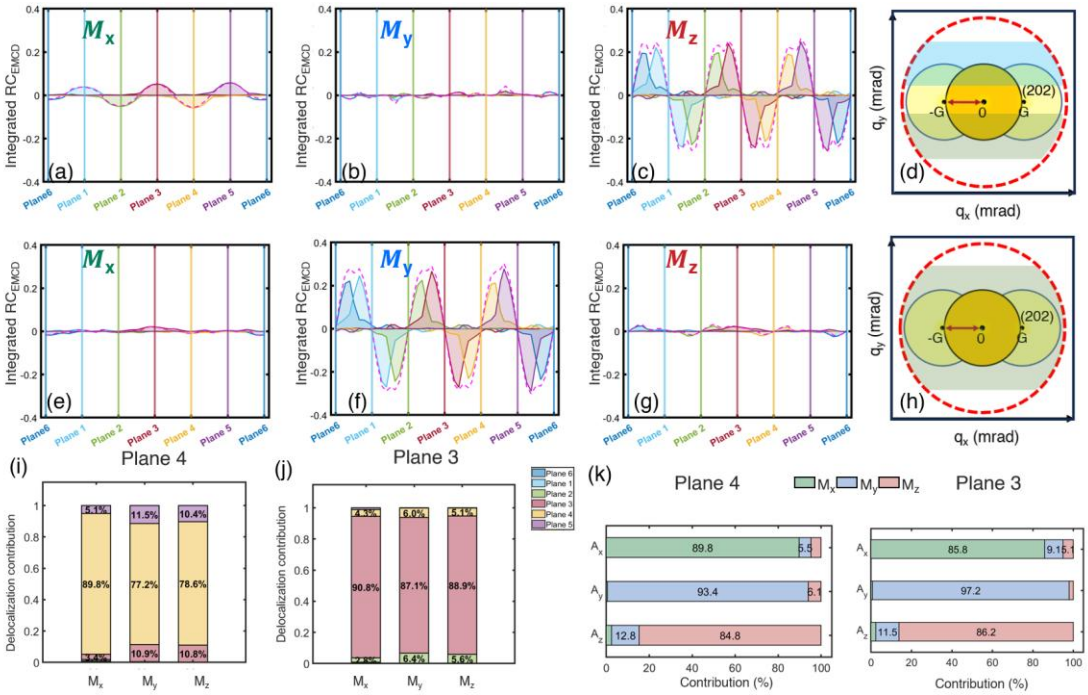


Figure S3 Beam-shift-dependent profiles of integrated relative dynamical diffraction coefficient of electron magnetic circular dichroism (RC_{emcd}) of the (a) $M_x(E)$, (b) $M_y(E)$ and (c) $M_z(E)$ components calculated from the difference in the integrated RC_{emcd} between the red and blue areas in q_y in the (d) schematic diffraction patterns under the three-beam condition (3BC). Beam shift-dependent profiles of integrated RC_{emcd} of the (e) $M_x(E)$, (f) $M_y(E)$ and (g) $M_z(E)$ components calculated from the integrated RC_{emcd} within the red area in q_y in the (h) schematic diffraction patterns under the 3BC. Colored filled lines show contributions from each atomic plane, while dashed lines represent total signals. The dashed red circles indicate the spectrometer entrance aperture. Delocalization contributions of the Fe (202) plane labeled 1 through 6 to the target planes (i) #4 and (j) #3 shows the dominant contribution localized at the corresponding plane itself. (k) Quantitative comparison of the signal crosstalk, showing the relative contributions of the $M(E)$, $M_y(E)$, and $M_z(E)$ components for each extraction strategy at the target planes 4 and 3. The data confirms the dominance of the target magnetic component in its respective optimized configuration.

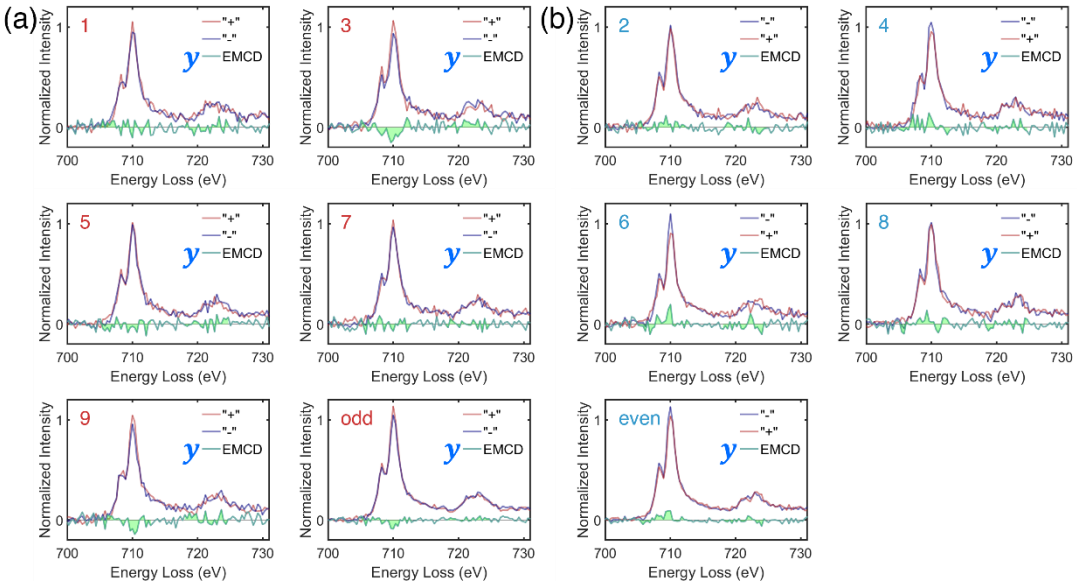


Figure S4 The raw-data positive "+" electron energy-loss (EEL) spectra in red, the negative "-" EEL spectra in blue and the electron magnetic circular dichroism (EMCD) spectra in green of (a) each odd-numbered Fe (202) planes labeled 1 through 9 and the sum, as well as (b) each even-numbered Fe (202) planes labeled 2 through 8 and the sum, extracted from four-dimensional EMCD dataset of $YFeO_3$ under the three-beam condition with the $\mathbf{G}_{(202)}$ systematic reflections excited using the A_y analysis strategy, which mainly represent the in-plane $M_y(E)$ component of three-dimensional magnetization vectors along the y axis as $[9\bar{2}\bar{9}]$.

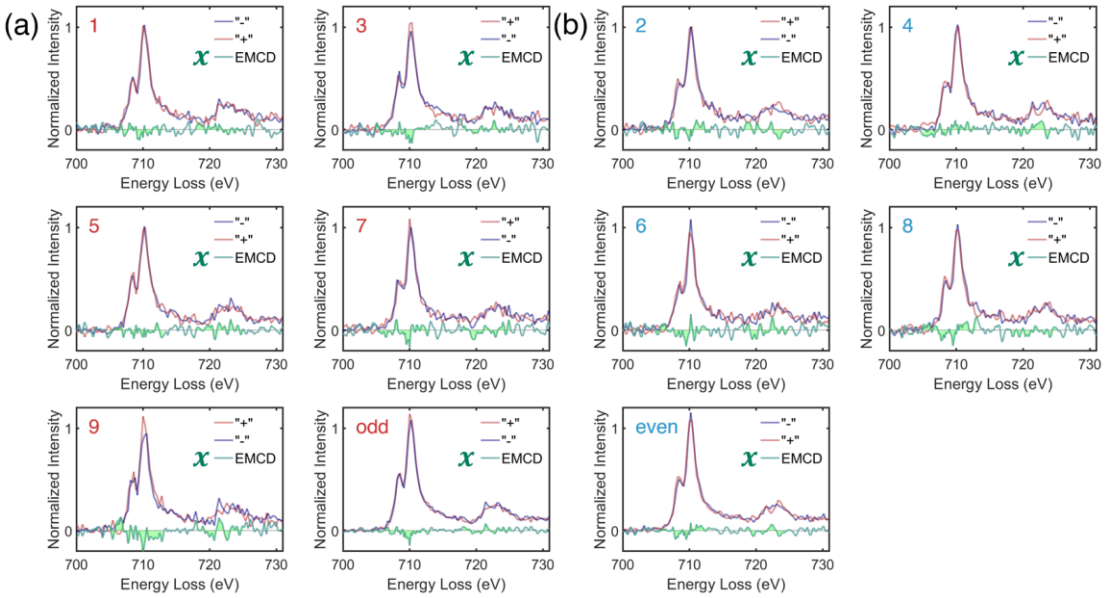


Figure S5 The raw-data positive "+" electron energy-loss (EEL) spectra in red, the negative "-" EEL spectra in blue and the electron magnetic circular dichroism (EMCD) spectra in green of (a) each odd-numbered Fe (202) planes labeled 1 through 9 and the sum, as well as (b) each even-numbered Fe (202) planes labeled 2 through 8 and the sum, extracted from four-dimensional EMCD dataset of $YFeO_3$ under the three-beam condition with the $\mathbf{G}_{(202)}$ systematic reflections excited using the A_x analysis strategy, which mainly represent the in-plane $M_x(E)$ component of three-dimensional magnetization vectors along the x axis as $\mathbf{G}_{(202)}$.

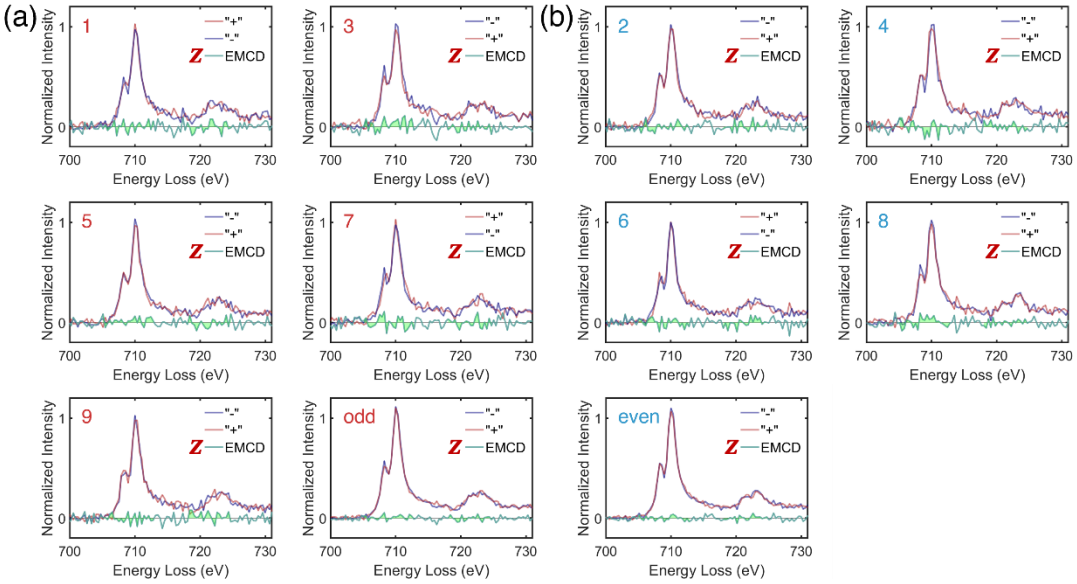


Figure S6 The raw-data positive "+" electron energy-loss (EEL) spectra in red, the negative "-" EEL spectra in blue and the electron magnetic circular dichroism (EMCD) spectra in green of (a) each odd-numbered Fe (202) planes labeled 1 through 9 and the sum, as well as (b) each even-numbered Fe (202) planes labeled 2 through 8 and the sum, extracted from four-dimensional EMCD dataset of $YFeO_3$ under the three-beam condition with the $\mathbf{G}_{(202)}$ systematic reflections excited using the A_z analysis strategy, which mainly represent the out-of-plane $M_z(E)$ component of three-dimensional magnetization vectors along the z axis as $[1,12,\bar{1}]$.

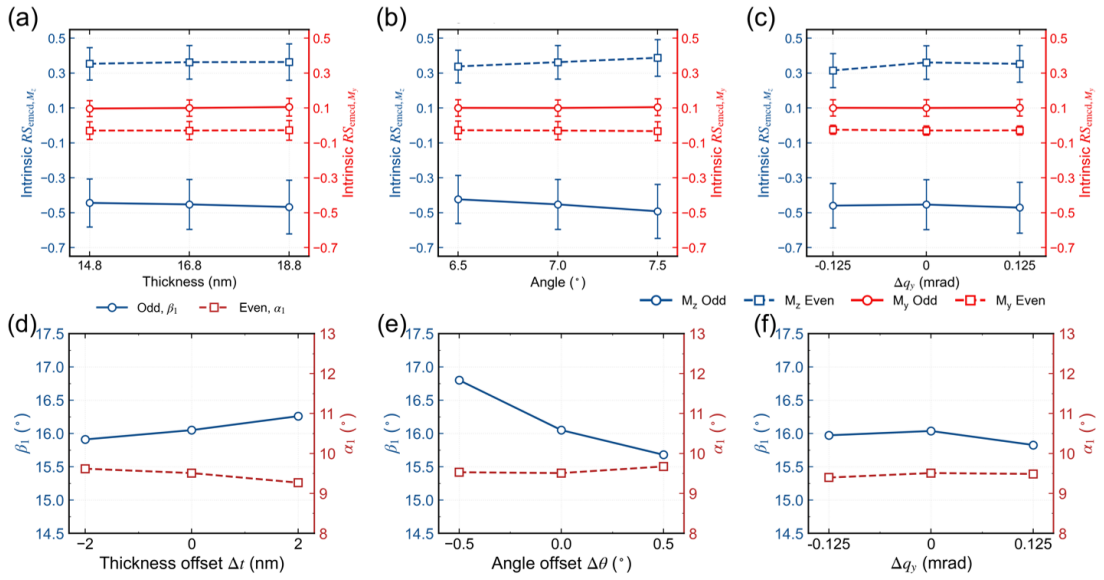


Figure S7 Sensitivity of intrinsic relative strength of electron magnetic circular dichroism (RS_{emcd}) values and spin-reorientation angles to sample thickness, tilting angle and virtual detector geometry. The intrinsic RS_{emcd} values for the M_z and M_y components (a,b,c), as well as the spin-reorientation angles α_1 for odd-numbered atomic planes and β_1 for even-numbered atomic planes (d,e,f), are calculated with variations in (a,d) sample thickness, (b,e) tilting angle away from Laue center, and (c,f) Δq_y selection in virtual detector geometry, which is defined and marked in the Extended Data Fig. 3i. The experimentally measured sample thickness of 16.8 nm with the variation of ±2 nm, the experimental tilting angle of 7° with the variation of ±0.5°, and the Δq_y selection of 0 mrad with the variation of ±0.125 mrad are selected.

Table S1 Error analysis of analyzed spin-reorientation angles with the assistance of dynamical diffraction simulation.

Reorientation angle	Error from experimental spectrum noise	Error from dynamical diffraction coefficients variation		Error from Δq_y variation (±0.125 mrad)	Total error
		Error from thickness variation (±2nm)	Error from angle variation (±0.5 °)		
α_1	7.8°	0.21°	0.75°	0.21°	7.84°
β_1	6.9°	0.24°	0.17°	0.11°	6.91°

Table S2. Intrinsic relative strength of electron magnetic circular dichroism (RS_{emcd}), derived spin-vector directions and projected canting angles for each spin sublattices and the representative atomic planes Nos. 1-3.

Spin Sublattice (Atomic Planes)	Intrinsic RSemcd (M_y)	Intrinsic RSemcd (M_z)	Derived Vector Direction (S_i) (Cartesian plane axis)	Approximating Miller index	Canting Angle	Canting Angle projected on ac-plane
Even-numbered	-0.029	0.364	[2.45, 0.29, −0.41]	$[91\bar{1}]$	11.6°	9.5°
Odd-numbered	0.100	-0.452	[−2.36, −0.49, 0.68]	$[\bar{5}\bar{1}1]$	19.5	16.1°
Plane 1	0.152	-0.560	[−2.31, −0.56, 0.77]	$[\bar{4}\bar{1}1]$	22.4°	18.3°
Plane 2	-0.112	0.682	[2.40, 0.41, −0.57]	$[61\bar{1}]$	16.3°	13.4°
Plane 3	0.073	-0.419	[−2.39, −0.43, 0.59]	$[\bar{6}\bar{1}1]$	17.0°	13.8°

Table S3 Spin Hamiltonian constants used for inferring the spin Hamiltonian energy terms[3]

Energy contribution	***Spin Hamiltonian constant***	***Value*** [3]
H_{ex}	J	$-4.77\ meV$
H_{DM}	$\boldsymbol{D}_{ij}$	$(0,0.62,0)\ meV$
H_z	$\mu_0 H, \widehat{\boldsymbol{H}}, \mu_{Fe}$	$2.5\ T,\ 3.6\ \mu_B$
$H_{sia,a}$	K_a	$0.0052\ meV$
$H_{sia,c}$	K_c	$0.0044\ meV$

5. References

1 Calmels, L. *et al.* Experimental application of sum rules for electron energy loss magnetic chiral dichroism. *Physical Review B* **76** (2007).

2 Rusz, J., Eriksson, O., Novák, P. & Oppeneer, P. M. Sum rules for electron energy loss near edge spectra. *Physical Review B* **76** (2007).

3 Amelin, K. *et al.* Terahertz absorption spectroscopy study of spin waves in orthoferrite YFeO 3 in a magnetic field. *Physical Review B* **98**, 174417 (2018).

4 Oberaigner, M. *et al.* Online thickness determination with position averaged convergent beam electron diffraction using convolutional neural networks. *Microscopy and Microanalysis* **29**, 427-436 (2023).